TOPOLOGICAL PHYSICS

Photonic axion insulator

Gui-Geng Liu[1,2]†, Subhaskar Mandal[1]†, Xiang Xi[3]†, Qiang Wang[4]†, Chiara Devescovi[5,6], Antonio Morales-Pérez[5,7], Ziyao Wang[8], Linyun Yang[8], Rimi Banerjee[1], Yang Long[1], Yan Meng[3], Peiheng Zhou[9], Zhen Gao[8,10], Yidong Chong[1,11], Aitzol García-Etxarri[5,12], Maia G. Vergniory[5,13,14], Baile Zhang[1,11]*

Axions, hypothetical elementary particles that remain undetectable in nature, can arise as quasiparticles in three-dimensional crystals known as axion insulators. Previous implementations of axion insulators have largely been limited to two-dimensional systems, leaving their topological properties in three dimensions unexplored in experiment. Here, we realize an axion insulator in a three-dimensional photonic crystal and probe its topological properties. Demonstrated features include half-quantized Chern numbers on each surface that resembles a fractional Chern insulator, unidirectional chiral hinge states forming topological transport in three dimensions, and arithmetic operations between fractional and integer Chern numbers. Our work experimentally establishes the axion insulator as a three-dimensional topological phase of matter and enables chiral states to form complex, unidirectional three-dimensional networks through braiding.

The hypothetical axionic particles, originally proposed to solve the strong charge-parity (CP) problem in the Standard Model and later predicted to constitute dark matter, continue to elude detection in nature (*1*–*7*). However, it is now understood that axions can emerge as collective excitations, or quasiparticles, in certain crystals known as axion insulators (AXIs) (*8*). Like their elementary counterparts, these quasiparticles are governed by an axion field, which introduces an additional term $\theta\mathbf{E}\cdot\mathbf{B}$ (where θ is the axion angle defined modulo 2π and $\mathbf{E}$, $\mathbf{B}$ are the electric and magnetic fields, respectively) into the electromagnetic Lagrangian, leading to "axion electrodynamics" with modified Maxwell's equations (*9*). In the crystal environment, the axion field can be quantized to act as a topological invariant that characterizes three-dimensional (3D) band topology, suggesting AXIs as a strong 3D topological phase of matter (*10*).

First, we compare a 3D axion insulator with the paradigmatic two-dimensional (2D) Chern insulator that is well known for its integer quantization (*11*, *12*). The 2D Chern insulator (Fig. 1A) is characterized by a bulk integer Chern number ($C = -1$ in the illustration), which dictates the number of chiral states propagating unidirectionally around the edges.

The 3D AXI (Fig. 1, B and C), by contrast, is characterized by a quantized axion angle $\theta = \pi$ in the bulk, which induces a half-quantized Chern number $C_s = \pm 1/2$ on all surfaces (*13*, *14*). Each surface thus behaves as a fractional Chern insulator (*15*–*23*) (recently discovered lattice analogs of the fractional quantum Hall effect), but not relying on strong interparticle correlations. The half-quantization gives rise to the following physical signatures. First, along each hinge between two adjacent surfaces with opposite half-quantized Chern numbers $C_s = \pm 1/2$, an integer (unit) number of chiral states arise (Fig. 1B), giving rise to topological chiral transport in 3D space. Second, if a 2D Chern insulator with an integer Chern number $C = -1$ is attached to the top surface of the 3D AXI, the half-quantized Chern number will be changed from $C_s = +1/2$ to $C_s = -1/2$ (Fig. 1C), thus redirecting the flow of chiral states (*24*).

An ideal AXI shows potential for achieving topological transport in three dimensions (*13*, *14*, *24*) and enabling physical operations between integer and fractional Chern numbers (Fig. 1, B and C). However, previously AXIs were predominantly implemented either on a 2D interface (*25*–*29*), such as between a 3D topological insulator and a ferromagnet, or in quasi-2D thin film geometries of intrinsic magnetic materials such as $MnBi_2Te_4$ (*30*–*32*).

We report the experimental realization of an AXI in a 3D photonic crystal. The crystal comprises a 3D stack of 2D photonic Chern insulators [photonic crystal implementations of Chern insulators (*33*)] with alternating Chern numbers of ±1 (*34*) (Fig. 2A). With mirror-reflection symmetry along the z axis, the crystal behaves as a photonic antiferromagnetic topological insulator (*34*), with side surfaces exhibiting a single-surface Dirac cone—a long-sought feature for 3D photonic topological insulators (*35*). When the mirror-reflection symmetry along the z axis is broken (*36*), the crystal becomes an ideal AXI (*14*), characterized by a bulk axion angle $\theta = \pi$ and gapped surfaces possessing surface Chern numbers of $C_s = \pm 1/2$. Through near-field microwave measurements, we map the chiral hinge states between adjacent surfaces with opposite surface Chern numbers, thus obtaining direct evidence for the "surface Chern insulator" behavior (*36*). We also demonstrate the redirection of the flow of chiral states due to the change in the surface Chern number from +1/2 to −1/2 by adding a layer with $C = -1$ from another photonic Chern insulator, confirming the interplay between fractional and integer Chern numbers. Further substantiating topological transport in three dimensions,

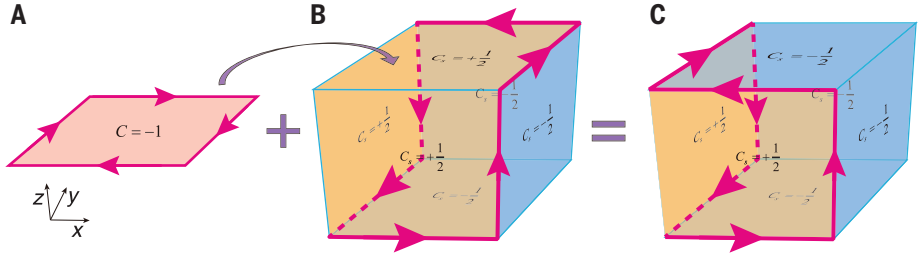

Fig. 1. Schematic comparison between a 2D Chern insulator and a 3D axion insulator. (**A**) A Chern insulator characterized by a Chern number ($C = -1$) carries chiral edge states along its edges. (**B**) An axion insulator exhibits surface Chern insulator phases, with each surface characterized by a half Chern number ($C_s = \pm 1/2$). Chiral hinge states occur between two adjacent surfaces with contrasting surface Chern numbers. (**C**) When the 2D Chern insulator with $C = -1$ is attached to the top surface of the axion insulator with $C_s = +1/2$, the surface Chern number of the top surface changes to $C_s = -1/2$, thus redirecting the flow of chiral hinge states around the top surface.

[1]Division of Physics and Applied Physics, School of Physical and Mathematical Sciences, Nanyang Technological University, Singapore, Singapore. [2]Research Center for Industries of the Future, Department of Electronic and Information Engineering, School of Engineering, Westlake University, Hangzhou, China. [3]School of Electrical Engineering and Intelligentization, Dongguan University of Technology, Dongguan, China. [4]National Laboratory of Solid State Microstructures, School of Physics, Collaborative Innovation Center of Advanced Microstructures, Nanjing University, Nanjing, China. [5]Donostia International Physics Center, Donostia-San Sebastian, Spain. [6]Institute for Theoretical Physics, ETH Zurich, Zurich, Switzerland. [7]Material and Applied Physics Department, University of the Basque Country (UPV/EHU), Donostia-San Sebastián, Spain. [8]Department of Electronic and Electrical Engineering, Southern University of Science and Technology, Shenzhen, China. [9]National Engineering Research Center of Electromagnetic Radiation Control Materials, Key Laboratory of Multi-spectral Absorbing Materials and Structures of Ministry of Education, University of Electronic Science and Technology of China, Chengdu, China. [10]State Key Laboratory of Optical Fiber and Cable Manufacture Technology, Department of Electronic and Electrical Engineering, Guangdong Key Laboratory of Integrated Optoelectronics Intellisense, Southern University of Science and Technology, Shenzhen, China. [11]Centre for Disruptive Photonic Technologies, The Photonics Institute, Nanyang Technological University, Singapore, Singapore. [12]IKERBASQUE, Basque Foundation for Science, Bilbao, Spain. [13]Max Planck Institute for Chemical Physics of Solids, Dresden, Germany. [14]Département de Physique et Institut Quantique, Université de Sherbrooke, Sherbrooke, Canada.
*Corresponding author. Email: blzhang@ntu.edu.sg
†These authors contributed equally to this work.

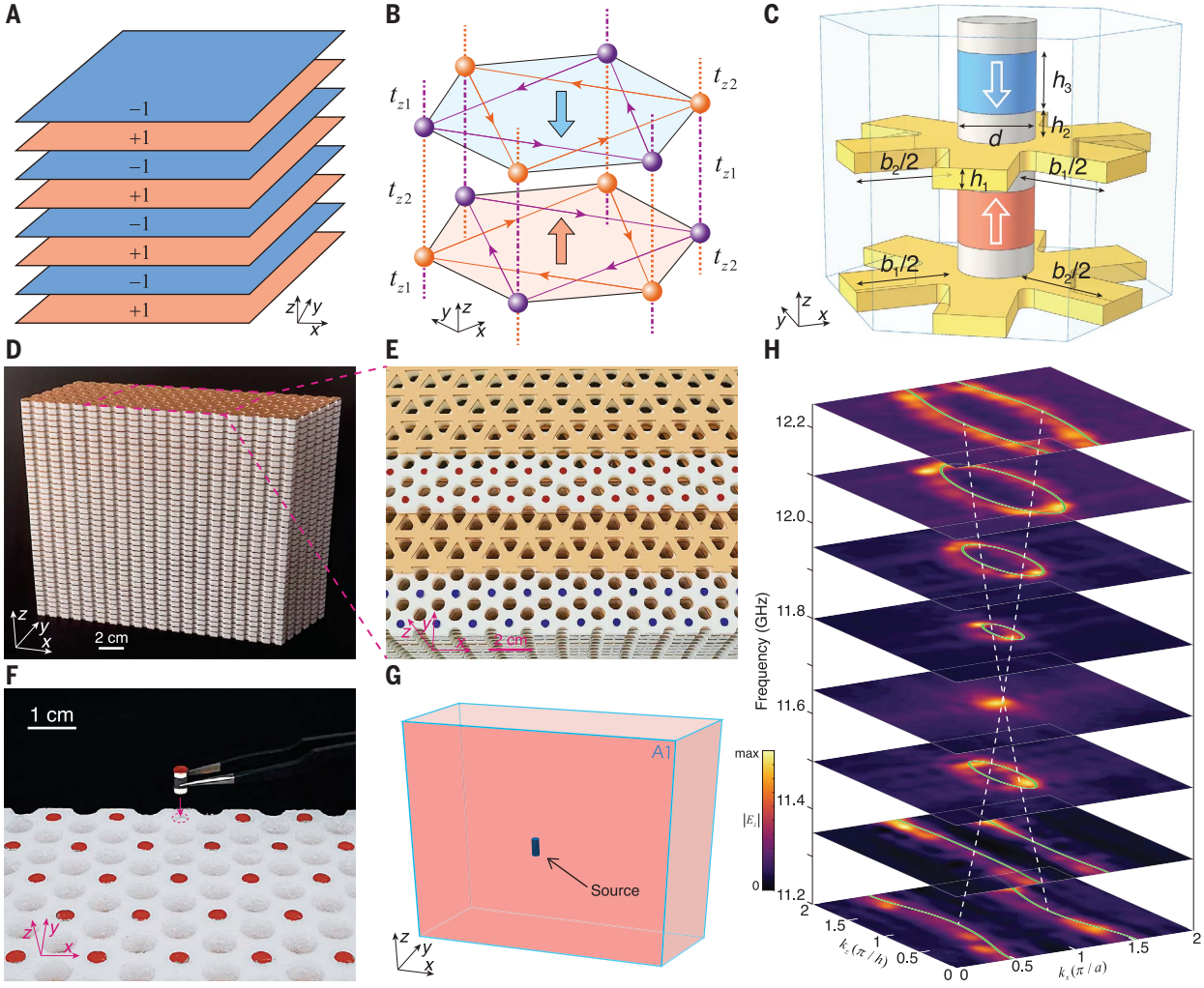

Fig. 2. Construction of a photonic topological antiferromagnet. (**A**) Strategy for constructing a topological antiferromagnet. (**B**) Schematic of the tight-binding model that stacks 2D Haldane model layers with opposite magnetic fluxes in adjacent layers. (**C**) Design of the unit cell of the 3D photonic crystal. Each gyromagnetic rod (red or blue cylinder) is biased by an average external magnetic field of 0.18 T produced by a pair of permanent magnets (gray cylinders), with the magnetization direction represented by a white arrow. The lattice constant in the *x*-*y* plane is a = 16 mm. The periodicity along z is h = 14 mm. The dimensions are d = 4 mm, h_1 = 1 mm, h_2 = 1.5 mm, h_3 = 3 mm. Here, $b_1 = b_2$ = 10 mm. (**D**) Photograph of a fabricated experimental sample with 40 layers in the z direction and 20 × 6 unit cells in the *x*-*y* plane. (**E**) Close-up view of the sample. The first two copper plates and one gyromagnetic rod layer on the top have been shifted for clarity. The coupling holes on the two adjacent copper plates have the same size. (**F**) Close-up view for one layer of gyromagnetic rods. The gyromagnetic rods and permanent magnets are embedded in dielectric foam to fix their positions. The permanent magnets are coated with high-conductivity materials. (**G**) Experimental setup for measurements of the surface states. (**H**) Measured surface dispersion on the A1 surface at different frequencies. Green lines indicate the simulated isofrequency contours. White dashed lines are guides to the eye that indicate the conical dispersion near the single-surface Dirac point.

we demonstrate the intricate braiding of chiral states to form a variety of 3D unidirectional networks, including knots and links, which cannot be projected to two dimensions.

Photonic single-surface Dirac cone

To construct the antiferromagnetic stacking (Fig. 2A), we consider the tight-binding model (Fig. 2B), which consists of stacked 2D Haldane model layers with alternating magnetic flux directions (i.e., alternating Chern numbers of ±1), with adjacent layers coupled through alternating interlayer hoppings t_{z1} and t_{z2} [see supplementary text for more details of the tight-binding model (*37*)]. Initially, we set $t_{z1} = t_{z2}$ to preserve the mirror-reflection symmetry along the z axis. This symmetry produces a nontrivial mirror Chern number that protects a single-surface Dirac cone on the zigzag side surfaces in a finite sample (*38*), while the top and bottom surfaces remain gapped [see supplementary text and fig. S1 for more detailed calculations (*37*)].

The 3D tight-binding model can be implemented in a 3D photonic crystal (Fig. 2C), in which the designed unit cell of the photonic crystal is composed of two gyromagnetic rods, sandwiched between and biased by two pairs of permanent magnets alongside two metallic plates perforated with holes. Triangular holes located at two sets of inequivalent corners of the hexagonal unit cell are perforated onto the metallic plates with side lengths of b_1 and b_2 to enable interlayer coupling. By ensuring $b_1 = b_2$, mirror-reflection symmetry is maintained along the z axis. These adjacent gyromagnetic rods are magnetically biased in opposite directions to achieve the antiferromagnetic configuration (*30*), which gaps the 3D Dirac point in the photonic crystal and opens a complete bulk bandgap from 11.19 to 12.58 GHz [see fig. S5 for details (*37*)]. Surface states in the zigzag side surfaces exhibit a single Dirac cone,

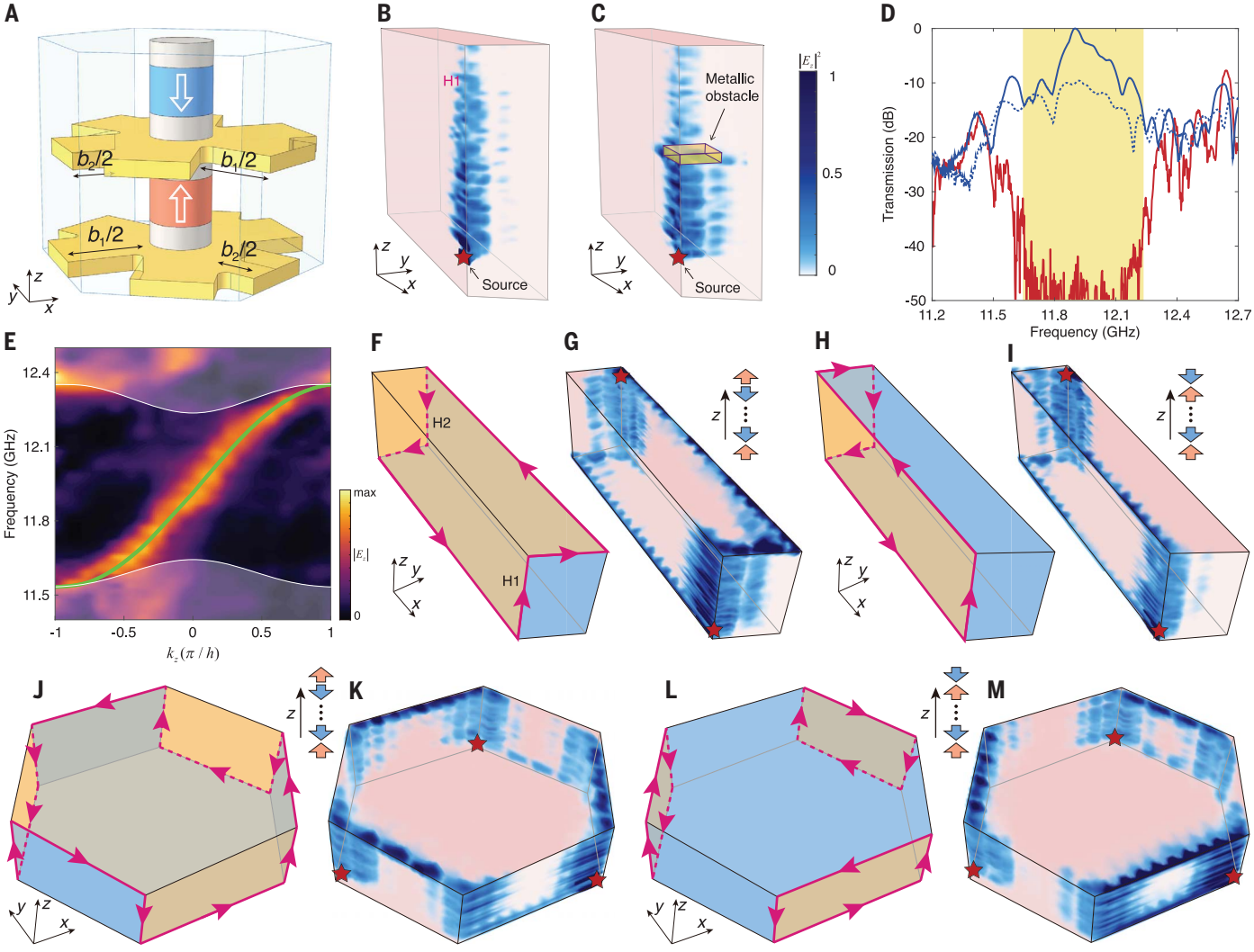

Fig. 3. Photonic axion insulator with chiral hinge states. (**A**) Unit cell of the photonic crystal. The parameters are the same as those in Fig. 2C except b_1 = 10 mm and b_2 = 5 mm. The coupling holes on the two adjacent copper plates have different sizes, thus breaking the mirror-reflection symmetry along the *z* axis. (**B** and **C**) Measured field distributions excited by a point source at 11.9 GHz near the H1 hinge. A large copper plate with dimensions of 6 mm in the *z* direction and 2 × 2 unit cells in the *x*-*y* plane is placed near the hinge as a metallic obstacle in (C). The sample has 40 layers in the *z* direction and 20 × 6 unit cells in the *x*-*y* plane. The decay of electric fields results from the material losses. (**D**) Measured transmission spectra near the H1 hinge. The red solid line denotes backward transmission. The blue solid and dashed lines denote forward transmission without and with a metallic obstacle, respectively. The yellow rectangle indicates the simulated complete gap of the bulk and surface states from 11.65 to 12.24 GHz. (**E**) Measured hinge dispersion on the H1 hinge. The green curve and white region represent the simulated hinge states and projected bulk and surface states. (**F**) Illustration of the trajectory of chiral hinge states on a parallelogram-shaped photonic crystal with an odd number of photonic Chern insulator layers. Yellow and blue surfaces indicate surface Chern numbers of +1/2 and −1/2, respectively. (**G**) Measured field distribution in the sample shown in (F), excited by the point sources (red stars). The sample has 39 layers in the z direction and 20 × 6 unit cells in the *x*-*y* plane. (**H** and **I**) Similar to (F) and (G) but with an even number of photonic Chern insulator layers. The sample has 40 layers in the *z* direction and 20 × 6 unit cells in the *x*-*y* plane. (**J** to **M**) Similar to (F) to (I) but for a hexagonal prism structure. The hexagonal prism sample has 10 unit cells as the side width and 11 layers in the *z* direction for panels (J) and (K), and 10 layers in the *z* direction for panels (L) and (M), respectively. The color scale of $|E_z|^2$ is linear.

protected by the nontrivial mirror Chern number [see supplementary text and figs. S6 to S8 for the topological invariant calculation and band simulation (*37*)]. Such a photonic single-surface Dirac cone has been long sought after for 3D photonic topological insulators (*35*).

Following this design, we construct the experimental sample shown in Fig. 2, D to F. To probe the surface states, the A1 surface of the photonic crystal (parallel to the *x*-*z* plane; see Fig. 2G) is covered with copper cladding to prevent wave leakage into the surrounding environment, whereas the other surfaces are wrapped with microwave absorbers. A point source is placed near the center of the A1 surface to excite surface states. The field distributions are mapped using a near-field scanning probe [see supplementary text (*37*)] and then Fourier-transformed to obtain the surface dispersion contour. The measured surface states form a single Dirac cone near 11.66 GHz (Fig. 2H), which is in excellent agreement with theoretical predictions and simulations (see figs. S1B and S6A).

Design of photonic axion insulator

We then break the mirror-reflection symmetry along the *z* axis by setting $t_{z1} \neq t_{z2}$ in the tight-binding model. In the photonic crystal design, this can be achieved by adjusting the hole sizes to make $b_1 \neq b_2$, for example, b_1 = 10 mm, b_2 = 5 mm

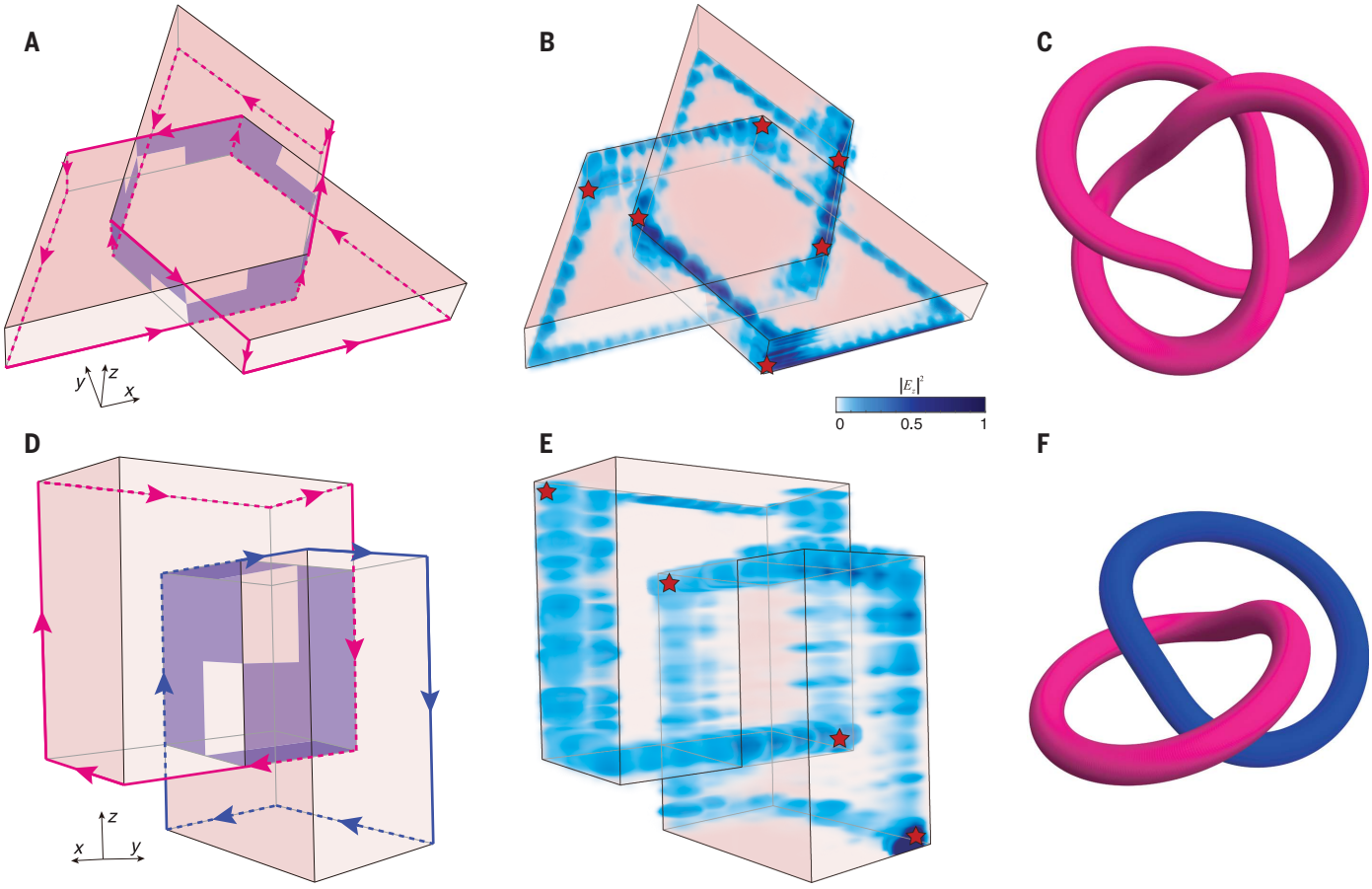

Fig. 4. Braiding of chiral hinge states. (**A** and **D**) Illustration of the photonic crystal design with chiral hinge states performing a trefoil knot and a Hopf link, respectively. The design in (A) has 11 layers in the *z* direction, and its length in the *x* direction consists of 32 unit cells. The design in (D) is formed by merging two parallelogram-shaped prisms, each with 15 layers in the *z* direction and dimensions in the *x*-*y* plane of 10 × 6 unit cells. (**B** and **E**) Corresponding measured field distributions of chiral hinge states illustrated in (A) and (D), respectively. (**C** and **F**) Corresponding topology diagrams. The color scale of $|E_z|^2$ is linear.

(Fig. 3A). In this scenario, the photonic crystal becomes an AXI, with (i) its bulk characterized by the axion angle $\theta = \pi$, (ii) all surfaces being gapped and possessing a half-surface Chern number of $C_s = \pm 1/2$, and (iii) chiral hinge states spanning 11.53 to 12.35 GHz [see supplementary text and figs. S2 to S6 for more details with tight-binding analysis and numerical simulations (*37*)]. Intuitively, the half-quantized surface Chern number on the side surfaces can be understood to arise from gapping the single-surface Dirac cone, similar to the previous surface gapping in 3D topological insulators (*25*–*29*, *39*, *40*). The half-surface Chern number on the top and bottom surfaces requires further analysis, which can be found in figs. S4, S6, and S8.

Measurements of chiral hinge states

To measure the chiral hinge states [see fig. S10 for the fabricated sample (*37*)], we cover the two surfaces adjacent to the hinge H1 (Fig. 3B) with copper claddings while the other surfaces are wrapped with microwave absorbers. By placing a point source near the hinge H1 and scanning the excited fields throughout the sample, we find that the fields at 11.9 GHz only propagate along the $+z$ direction near the hinge H1, and with almost no fields observed propagating backward (Fig. 3B). Additionally, even with a large copper plate inserted as a metallic obstacle, the hinge states are observed to bypass the obstacle and continue their propagation without any backscattering (Fig. 3C), thus confirming the unidirectional propagation of the chiral hinge states and their robustness against obstructions.

We also measure the frequency-dependent transmission spectra of hinge states by positioning two source antennas at two ends of hinge H1, respectively (Fig. 3D). For the backward transmission (red line in Fig. 3D), a dip is observed around 11.6 to 12.2 GHz, manifesting a complete gap of the surface and bulk states. However, the forward transmission (blue solid line in Fig. 3D) shows a strong signal, ~40 dB greater than the backward transmission at mid-gap frequencies. Even with a large obstacle on the hinge (for the case in Fig. 3C), the forward transmission (blue dashed line in Fig. 3D) maintains a level ~30 dB greater than the backward transmission within the gap. Furthermore, by performing a Fourier transform of the measured fields near hinge H1, we obtain the dispersion of the hinge states, which display positive group velocities along the k_z direction, indicative of chiral propagation (Fig. 3E; see more details and results in fig. S9).

Arithmetic operation between fractional and integer Chern numbers

To map out the closed trajectories of the chiral hinge states, we first consider a sample with a parallelogram-like prism structure containing an odd number of photonic Chern insulator layers (Fig. 3F). At hinges H1 and H2, the hinge states propagate in the $+z$ and $-z$ directions, respectively. The top and bottom surfaces have surface Chern numbers of +1/2 and −1/2 (indicated in yellow and blue for all surfaces in Fig. 3F), respectively. The hinge states propagate anticlockwise within both the top and bottom surfaces, forming a closed loop. To observe this experimentally, we cover all surfaces of the sample with copper claddings and scan the fields excited by two point sources [see supplementary text for experimental details (*37*)]. The measured results (Fig. 3G) show a closed

loop, in agreement with the predictions. We note that other 3D topological phases can also host chiral hinge states, though not on all hinges (*41*).

We then attach one more photonic Chern insulator layer with Chern number −1 to the top surface of the 3D AXI (Fig. 3H). This causes the surface Chern number on the top surface to change from +1/2 to −1/2, and thus the propagation direction of chiral hinge states in the top surface become clockwise. The resulting closed-loop configuration of the chiral hinge states (Fig. 3H) is verified through experimental mapping (Fig. 3I).

We also construct a hexagonal prism-shaped sample with an odd number of photonic Chern insulator layers (Fig. 3J). A closed loop traversing all vertical hinges is formed (Fig. 3, J and K). By adjusting the sample to be an even number of layers, both the top and bottom surfaces have the surface Chern number −1/2, generating three isolated loops at the side surfaces (Fig. 3L), which is further experimentally confirmed (Fig. 3M). Hence, each of those three side surfaces acts as a conventional 2D Chern insulator (*11*, *12*).

Braiding of chiral hinge states

As a final demonstration of the distinctive topological transport features of the AXI, we implement samples where the chiral hinge states are braided into complex knots and links in 3D space. Figure 4, A and B, depicts a photonic crystal in which chiral hinge states exhibit a trefoil knot in 3D space (the topology is illustrated in Fig. 4C). Copper plates are integrated into the crystal to facilitate the self-braiding of chiral hinge states. The detailed construction is illustrated in fig. S11, A to H. We also engineer a composite structure by merging two parallelogram-shaped prisms (Fig. 4D), creating a Hopf link (Fig. 4E) (the topology is illustrated in Fig. 4F). For more details of the design and the analysis, see fig. S11, I to N.

Outlook

The above results clearly demonstrate the realization of an AXI in a 3D photonic crystal. The interaction between fractional and integer Chern numbers opens new avenues in topological physics, offering insights that could guide similar demonstrations in condensed-matter or cold-atom systems. Though demonstrating fixed values of quantized axion field angle $\theta = \pi$ and half Chern numbers of $\pm 1/2$, other values could potentially be achieved through the engineering of spins for axion quasiparticles (*42*). Furthermore, the current setup may evolve to exhibit Majorana-like chiral hinge states (*43*), whose braiding may be valuable for topological quantum computing (*44*). Although implemented at microwave frequencies, other photonic realizations may also be possible at higher frequencies, given the successful realization of several 2D photonic Chern insulators at optical frequencies (*45*–*47*). Notably, current axion haloscopes seek to detect axions by converting them into detectable microwave photons under a strong magnetic field (*4*–*7*, *9*). Our photonic AXI could serve as a tabletop platform to investigate axion-photon interactions and other fundamental aspects of axion electrodynamics (*8*, *48*).

REFERENCES AND NOTES

1. R. D. Peccei, H. R. Quinn, *Phys. Rev. Lett.* **38**, 1440–1443 (1977).
2. J. E. Kim, G. Carosi, *Rev. Mod. Phys.* **82**, 557–601 (2010).
3. J. Preskill, M. B. Wise, F. Wilczek, *Phys. Rev. B Condens. Matter* **120**, 127 (1983).
4. D. J. Marsh, *Phys. Rep.* **643**, 1–79 (2016).
5. E. Braaten, H. Zhang, *Rev. Mod. Phys.* **91**, 041002 (2019).
6. F. Chadha-Day, J. Ellis, D. J. E. Marsh, *Sci. Adv.* **8**, eabj3618 (2022).
7. Y. K. Semertzidis, S. Youn, *Sci. Adv.* **8**, eabm9928 (2022).
8. F. Wilczek, *Phys. Rev. Lett.* **58**, 1799–1802 (1987).
9. P. Sikivie, *Phys. Rev. Lett.* **51**, 1415–1417 (1983).
10. D. M. Nenno, C. A. C. Garcia, J. Gooth, C. Felser, P. Narang, *Nat. Rev. Phys.* **2**, 682–696 (2020).
11. M. Z. Hasan, C. L. Kane, *Rev. Mod. Phys.* **82**, 3045–3067 (2010).
12. X.-L. Qi, S.-C. Zhang, *Rev. Mod. Phys.* **83**, 1057–1110 (2011).
13. N. Varnava, D. Vanderbilt, *Phys. Rev. B* **98**, 245117 (2018).
14. Y. Xu *et al*., *Nature* **586**, 702–707 (2020).
15. E. M. Spanton *et al*., *Science* **360**, 62–66 (2018).
16. Y. Xie *et al*., *Nature* **600**, 439–443 (2021).
17. J. Cai *et al*., *Nature* **622**, 63–68 (2023).
18. H. Park *et al*., *Nature* **622**, 74–79 (2023).
19. Y. Zeng *et al*., *Nature* **622**, 69–73 (2023).
20. F. Xu *et al*., *Phys. Rev. X* **13**, 031037 (2023).
21. J. Léonard *et al*., *Nature* **619**, 495–499 (2023).
22. Z. Lu *et al*., *Nature* **626**, 759–764 (2024).
23. C. Wang *et al*., *Science* **384**, 579–584 (2024).
24. B. J. Wieder, B. A. Bernevig, arXiv:1810.02373 [cond-mat.mes-hall] (2018).
25. L. Wu *et al*., *Science* **354**, 1124–1127 (2016).
26. M. Mogi *et al*., *Sci. Adv.* **3**, eaao1669 (2017).
27. M. Mogi *et al*., *Nat. Mater.* **16**, 516–521 (2017).
28. D. Xiao *et al*., *Phys. Rev. Lett.* **120**, 056801 (2018).
29. D. Zhuo *et al*., *Nat. Commun.* **14**, 7596 (2023).
30. M. M. Otrokov *et al*., *Nature* **576**, 416–422 (2019).
31. C. Liu *et al*., *Nat. Mater.* **19**, 522–527 (2020).
32. A. Gao *et al*., *Nature* **595**, 521–525 (2021).
33. Z. Wang, Y. Chong, J. D. Joannopoulos, M. Soljačić, *Nature* **461**, 772–775 (2009).
34. I. C. Fulga, N. Avraham, H. Beidenkopf, A. Stern, *Phys. Rev. B* **94**, 125405 (2016).
35. L. Lu *et al*., *Nat. Phys.* **12**, 337–340 (2016).
36. C. Yue *et al*., *Nat. Phys.* **15**, 577–581 (2019).
37. Materials, methods, and additional information are available as supplementary materials.
38. F. Schindler *et al*., *Sci. Adv.* **4**, eaat0346 (2018).
39. R. Lu *et al*., *Phys. Rev. X* **11**, 011039 (2021).
40. M. Mogi *et al*., *Nat. Phys.* **18**, 390–394 (2022).
41. X. Ni, Z. Xiao, A. B. Khanikaev, A. Alù, *Phys. Rev. Appl.* **13**, 064031 (2020).
42. S. Li, M. Gong, Y.-H. Li, H. Jiang, X. C. Xie, *Nat. Commun.* **15**, 4250 (2024).
43. Q. Yan, H. Li, J. Zeng, Q.-F. Sun, X. C. Xie, *Commun. Phys.* **4**, 239 (2021).
44. C. Nayak, S. H. Simon, A. Stern, M. Freedman, S. Das Sarma, *Rev. Mod. Phys.* **80**, 1083–1159 (2008).
45. B. Bahari *et al*., *Science* **358**, 636–640 (2017).
46. Y. G. N. Liu, P. S. Jung, M. Parto, D. N. Christodoulides, M. Khajavikhan, *Nat. Phys.* **17**, 704–709 (2021).
47. J. Jin *et al*., arXiv:2304.09385 [physics.optics] (2023).
48. C. Devescovi *et al*., *Nat. Commun.* **15**, 6814 (2024).
49. G.-G. Liu *et al*., Data for 3D Photonic Crystal, DR-NTU (Data) (2024); https://doi.org/10.21979/N9/XSPEHE.

ACKNOWLEDGMENTS

Funding: The authors acknowledge funding from Singapore National Research Foundation Competitive Research Program grant NRF-CRP23-2019-0007 and Singapore Ministry of Education Academic Research Fund Tier 2 grant MOE-T2EP50123-0007. Q.W. acknowledges funding from the Fundamental Research Funds for the Central Universities grant no. 2024300369 and National Natural Science Fund for Excellent Young Scientists Fund Program (Overseas). G.-G.L. acknowledges funding from Research Center for Industries of the Future (RCIF) at Westlake University grant no. 210000006022312 and Westlake Education Foundation grant no. 103110736022301. P.Z. acknowledges funding from National Natural Science Foundation of China grant nos. 52022018, 52021001, 6101020101, and 62175215. Z.G. acknowledges funding from the National Natural Science Foundation of China under grant nos. 62375118, 62361166627, and 12104211; Guangdong Basic and Applied Basic Research Foundation under grant no.2024A1515012770; Shenzhen Science and Technology Innovation Commission under grant nos. 20220815111105001 and 20230807000209; and High level of special funds under grant no. G03034K004. Y.L. gratefully acknowledges the support of the Eric and Wendy Schmidt AI in Science Postdoctoral Fellowship, a Schmidt Futures programme. A.G.-E., M.G.V., A.M.-P, and C.D. acknowledge support from the Spanish Ministerio de Ciencia e Innovación grant PID2022-142008NB-I00. A.G.-E., A.M.-P., and C.D. acknowledge support from the Gipuzkoa Provincial Council within the QUAN-000021-01 project, as well as the Basque Government Elkartek program (KK-2023/00016). A.G.-E. and M.G.V. acknowledge funding from the IKUR Strategy under the collaboration agreement between the Ikerbasque Foundation and DIPC on behalf of the Department of Education of the Basque Government, Programa de ayudas de apoyo a los agentes de la Red Vasca de Ciencia, Tecnología e Innovación acreditados en la categoría de Centros de Investigación Básica y de Excelencia (Programa BERC) from the Departamento de Universidades e Investigación del Gobierno Vasco and Centros Severo Ochoa AEI/CEX2018-000867-S from the Spanish Ministerio de Ciencia e Innovación. M.G.V. acknowledges financial support from the Canada Excellence Research Chairs Program for Topological Quantum Matter and Deutsche Forschungsgemeinschaft (DFG, German Research Foundation) GA 3314/1-1 – FOR 5249 (QUAST) and partial support from European Research Council (ERC) grant agreement no. 101020833. C.D. and A.M.-P. acknowledge discussions with I. Robredo and B. Bradlyn. **Author contributions:** G.-G.L. and Q.W. initiated the project. S.M., Q.W., G.-G.L., C.D., A.M.-P., R.B., A.G.-E., and M.G.V. performed the theoretical explanation and developed the tight-binding model simulations. G.-G.L. performed the simulation, designed the experiments, and analyzed the data. X.X., Z.W., Z.G., and G.-G.L. carried out the measurements. All authors discussed the results and contributed to the writing of the manuscript. B.Z. supervised the project. **Competing interests:** The authors declare no competing interests. **Data and materials availability:** All data are available in the manuscript or the supplementary materials or have been deposited at DR-NTU (Data) (*49*).

SUPPLEMENTARY MATERIALS

science.org/doi/10.1126/science.adr5234
Supplementary Text
Figs. S1 to S14
References (*50*–*57*)

Submitted 6 July 2024; accepted 11 November 2024
10.1126/science.adr5234